AIAA/ASME/SIAM/APS
1st NATIONAL
FLUID DYNAMICS CONGRESS
JULY 25-28, 1988
CINCINNATI, OHIO

PART 1

A COLLECTION OF TECHNICAL PAPERS
CINCINNATI, OHIO
JULY 25-28, 1988

SOME OBSERVATIONS ON THE INFLUENCE OF LONGITUDINAL VORTICES IN A LID-DRIVEN CAVITY FLOW

88-3654-CP

Ajay K. Prasad,[1] Chin-Yuan Perng[1] and Jeffrey R. Koseff[2]

Environmental Fluid Mechanics Laboratory
Department of Civil Engineering
Stanford University
Stanford, CA 94305

Abstract

This paper describes a joint physical and numerical investigation into a lid-driven cavity flow at a Reynolds number (based on the cavity width and the lid-velocity) of 3200, and Spanwise Aspect Ratios (SAR; the ratio of the cavity length to its width) of 1:1, 0.5:1 and 0.25:1. The experimental techniques consisted of flow visualization (with polystyrene micro-spheres) of specific planes in the cavity, as well as velocity measurements using laser-Doppler anemometry along the horizontal and vertical center-lines at the symmetry plane of the cavity. The numerical results were obtained using SEAFLOS1-I, which employs the implicit Euler scheme for time-stepping and a quadratic upwind scheme (QUICK) to finite difference the convective terms in the Navier-Stokes equations. First, we demonstrate that SEAFLOS1-I reproduces the qualitative and quantitative aspects observed and measured in our physical experiments. We then use the spatially-intensive data of the simulations to complement the temporally-intensive data of the experiments, in order to examine more closely the characteristics of the Taylor-Görtler-Like (TGL) vortices, and the interaction of the TGL vortices, the Downstream Secondary Eddy (DSE), and the corner vortices, with each other, and their influence on momentum transfer within the cavity.

Our observations reveal that the DSE is larger in the immediate vicinity of the corner vortices (found at the endwalls) and in the region of the TGL vortices. This is because the TGL vortices entrain fluid from the DSE. Because the formation of the TGL vortices is contingent on the presence of a concave separation surface at the DSE, the entrainment process described above results in a complex "feedback" process between the TGL vortices and the DSE. This leads to a temporal variation in the local size of the DSE and a spanwise meandering of the TGL vortices for cavities of SAR > 0.5:1.

Nomenclature

B	cavity width
D	cavity height or depth
L	cavity length or span
Re	Reynolds number based on lid-velocity and cavity width
U	velocity in the horizontal (X) direction
U_B	lid-velocity
V	velocity in the vertical (Y) direction
x	horizontal co-ordinate axis aligned with cavity width
X	non-dimensionalized x co-ordinate
y	vertical co-ordinate axis aligned with cavity depth
Y	non-dimensionalized y co-ordinate
z	horizontal co-ordinate axis aligned with cavity length
Z	non-dimensionalized z co-ordinate
ν	kinematic viscosity of water

Abbreviations

DAR	Depthwise Aspect Ratio
DSE	Downstream Secondary Eddy
DSW	Downstream Side Wall
SAR	Spanwise Aspect Ratio
TGL	Taylor-Görtler Like
USW	Upstream Side Wall

[1]Research Assistant, Department of Mechanical Engineering
[2]Assistant Professor, Department of Civil Engineering

Introduction

Shear-driven flows in cavities are often encountered in engineering situations, as in the case of rectangular cut-outs on the surface of aircraft bodies and heat-exchangers. Shear-driven cavity flows are also interesting from a more fundamental standpoint, because they are rich in complex, three-dimensional (3-d) phenomena. A special case of such flows is the lid-driven flow in a rectangular cavity. A regular geometry and well-posed boundary conditions make this flow an attractive test-case for numerical schemes, as described by de Vahl Davis and Mallinson,[1] Tuann and Olson,[2] and Koseff and Street.[3] As a result, over the years, this flow has been simulated repeatedly, but with a large variation in results. For example, the two-dimensional (2-d) simulations of Ghia et al.,[4] Olson and Tuann,[5] and Nallasamy and Krishna Prasad,[6] among others, were inconsistent in that the size of the Downstream Secondary Eddy (DSE) varied in trend and magnitude from one simulation to another as a function of the Reynolds number ($Re = U_B B/\nu$, where U_B is the lid-velocity, B is the width of the cavity, and ν is the kinematic viscosity of the working fluid). Second, numerically stable simulations at higher Re, which were facilitated by upwind-differencing the convective terms, often led to results containing spurious numerical diffusion.

In an effort to resolve some of the discrepancies reported in the literature, Koseff and Street[3,7,8] conducted a series of experiments in a lid-driven cavity flow. They confirmed that the flow exhibits both local and global 3-d features. Locally, they found that the Taylor-Görtler-Like (TGL) vortices, which form in the region of the DSE (Figure 1), and the corner vortices which form along the cavity endwalls, interact quite strongly with the primary circulation cell and thereby influence the distribution of momentum within the entire cavity. On a global scale, they found that the three-dimensionality results from the adjustment of the primary flow to the no-slip conditions imposed by the end-walls, resulting in a "weaker" flow as compared with a pure 2-d flow. In addition, they found that at a Spanwise Aspect Ratio (SAR: the ratio of the length L to the width B, (Figure 1)) of 3:1, the DSE

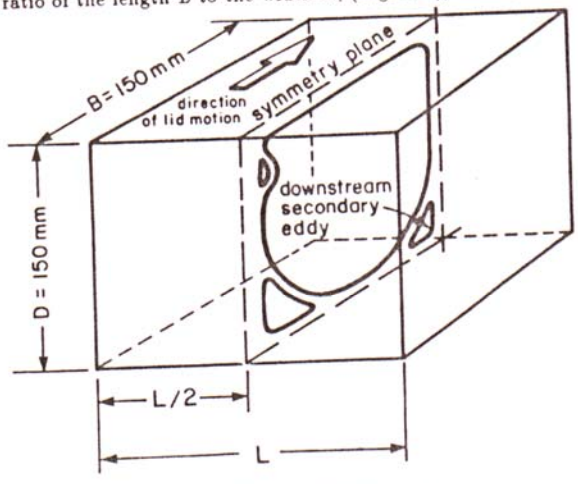

L = 150 mm (SAR = 1:1)
L = 75 mm (SAR = 0.5:1)
L = 37.5 mm (SAR = 0.25:1)

Figure 1 Definitions for the lid-driven cavity flow

increased in size as Re increased to 10,000, but at SAR's of 1:1 and 2:1 the DSE reduced in size with increasing Re, for $Re > 2000$. Furthermore, dye-streak studies seemed to indicate that spiralling spanwise motions were present in the DSE, leading to the entrainment of the fluid from the DSE into the corner vortex.

At the time Koseff and Street performed these experiments, no accurate 3-d numerical simulation of this flow existed. It was quite apparent, however, that because of the demonstrated (and in some sense, unexpected) complexity of this flow that the spatial limitations on the data available from the physical experiments was constraining a more complete understanding of the flow. Freitas et al.,[9,10] using the REMIXCS code, obtained the first 3-d simulation of the $Re = 3200$ flow which reproduced the TGL vortices observed in the physical experiments. However, their simulations proved to be computationally expensive. More recently, a time-accurate simulation scheme, the Stanford EnvironmentAl Fluid Mechanics LabOratory Simulator, Version 1, Implicit (SEAFLOS1-I) has been developed, which (as will be demonstrated) has not only reproduced all the observed flow features, but has also achieved excellent agreement with measurements from physical experiments. Moreover, SEAFLOS1-I has demonstrated a five-fold gain in computational speed over the REMIXCS code. Consequently, we are now able to combine the information from the spatially-intensive data of the numerical experiments, the temporally-intensive data of the physical experiments, and our flow-visualization photographs to gain a broader understanding of the physics of the lid-driven cavity flow. Specifically, we wish to examine more closely the characteristics of the TGL vortices, and the interaction of the TGL vortices, the DSE, and the corner vortices, with each other, and their influence on momentum transfer within the cavity.

The $Re = 3200$ flow, for which a significant amount of physical and numerical data exist, was chosen as the test-case. Physical experiments, using flow-visualization and laser-Doppler anemometer (LDA) velocity measurements, and numerical simulations were performed for this flow at SAR's of 0.25:1, 0.5:1 and 1:1. Our approach was first to validate and verify our numerical scheme by comparing time-averaged velocity profiles measured in the symmetry plane (see Figure 1) with those obtained from the numerical simulations. Once this was done successfully, the numerical code itself could be used as an experimental facility to explore the flows in a manner which was not feasible physically.

In this paper, the results from the joint physical and numerical experimental study are presented. The presentation of the main results is preceded by a description of our experimental facilities and instrumentation and a description of the code verification procedure. The paper ends with a summary and conclusions.

Experimental Facility and Instrumentation

Facility

Figure 2 shows the lid-driven cavity facility in its assembled form. It consists of two attached "shoe-boxes". The lower box, fabricated from 12.5 mm thick plexiglas, is the cavity area of interest, while the upper box houses the drive system. It consists of a variable speed motor connected by a chain drive to one of a pair of rollers. The "lid" is a copper belt, 0.08 mm thick, and is mounted on and driven by the two rollers. During operation, the belt continuously touches the upper edges of the lower box, thus minimizing the influx and outflow of fluid. The belt speed can be varied to produce Reynolds numbers up to 15,000. However, at a particular setting the belt speed is constant to $\pm 0.25\%$. The belt is in continuous contact with a heat exchanger plate, and the lower boundary of the cavity also consists of another such plate. By circulating water of the same temperature through both these plates, an isothermal condition can be maintained in the cavity. Furthermore, heat transfer to the surroundings through the vertical walls of the cavity is minimized by maintaining the operating temperature as close to the laboratory ambient temperature as possible, and by adding insulation in the form of double-glazing and styrofoam. These precautions are necessitated by the fact that a temperature differential between the upper and lower boundaries of the cavity as small as 0.05 K could lead to erroneous results.

In the experiments described herein, we maintained a Depthwise Aspect Ratio (DAR) of 1:1 (DAR $= D/B$, where D is the cavity depth; in these experiments $D = B = 150$ mm). By using false insert walls, we obtained spanwise-aspect-ratios of 0.25:1 ($L = 37.5$ mm), 0.5:1 ($L = 75$ mm), and 1:1 ($L = 150$ mm).

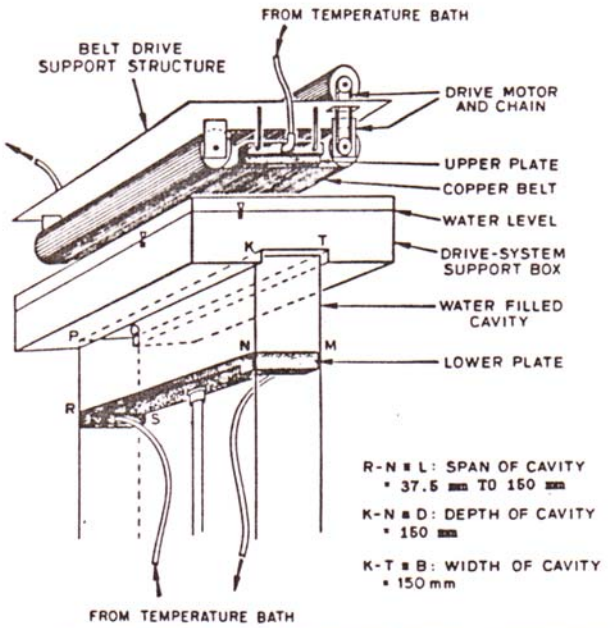

Figure 2 Schematic of lid-driven cavity (Reproduced from Koseff and Street)

Flow Visualization Techniques

Polystyrene micro-spheres were used to visualize the flow structures, in the manner described by Rhee et al.[11] These micro-spheres range in size from 100-200μm, have a high reflectivity, and a specific gravity of about 1.03. They, therefore, remain suspended in water for sufficiently long periods of time and can be easily advected by the flow, providing representative pathlines. It was found that the optimal concentration of the micro-spheres in water was about 0.1 gm/ltr. A 1000W projector lamp, together with a slit-and-lens assembly provided 3 mm thick sheets of light with which specific planes in the cavity were illuminated. Photographs were taken using 4-second exposures to extract flow details with sufficient clarity.

In order to help the reader identify the various planes in which the photographs were taken, we now introduce a suitable co-ordinate system (Figure 3). In this system, the origin is located at the geometric center of the cavity. Each of the three axes is non-dimensionalized by the appropriate cavity dimension, such that $X = x/B$, $Y = y/D$ and $Z = z/L$. Thus, the plane $Y = 0.5$ comprises the lid, whereas the

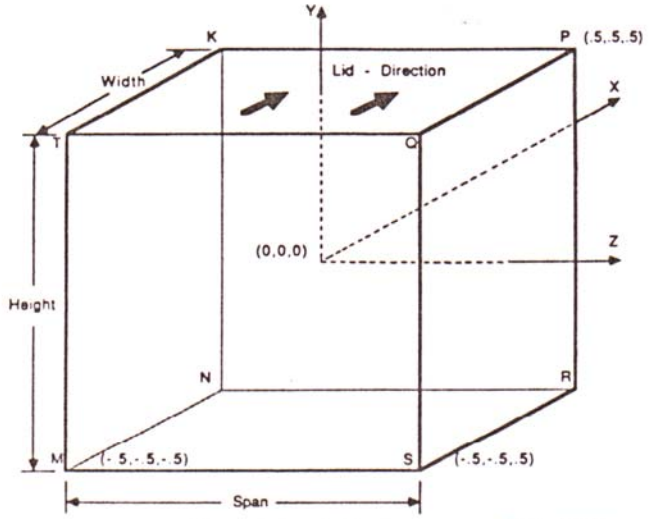

TQSM: Upstream Side Wall KPRN: Downstream Side Wall
KPQT: Lid NRSM: Lower Boundary
TKNM: Endwall QPRS: Endwall

Figure 3 Co-ordinate system for the lid-driven cavity flow

plane $Y = -0.5$ forms the lower cavity boundary. Similarly, the plane $X = 0.5$ and $X = -0.5$ form the Downstream and Upstream Side Walls respectively. The planes $Z = 0.5$ and $Z = -0.5$ represent the end-walls, while the symmetry plane is the plane $Z = 0$. As shown in Figures 1 and 3, the recirculating flow is set up by the lid-motion in the $Y = 0.5$ plane, in the positive X direction.

Velocity Measurements

Instantaneous velocity measurements in the symmetry plane along the horizontal and vertical center-lines were obtained using a two-component DANTEC 55X modular optical laser-Doppler anemometer (LDA) system, operated in the forward scatter mode. Each of the two channels used a DANTEC type 55N12 Frequency shifter and a DANTEC type 55N21 Frequency Tracker to perform the signal processing. A combination of a low tracker-frequency range and the amplification of the tracker-output voltage reduced the overall error in the measured velocity to about ±0.4 mm/s. An HP2100 data acquisition system was used to sample the velocity signal at a rate of 100 Hz, for a period of 5.46 minutes at each measuring point. The velocity signal was low-pass filtered at 40 Hz prior to digitization.

Numerical Simulation

SEAFLOS1-I Computer Code

SEAFLOS1-I solves a weak form of the Navier-Stokes equations in primitive variables using a finite-volume formulation and the staggered grid system. The implicit Euler scheme is used for time-stepping. SEAFLOS1-I incorporates two key features: (1) the ICCG (Incomplete Choleskey decomposition, Conjugate Gradient) method, and (2) a modified QUICK (Quadratic Upwind Interpolation for Convective Kinematics) formulation for non-uniform grid systems. In addition, an MG (Multigrid) version of SEAFLOS1-I is also available. The ICCG method and the MG technique are extremely efficient in solving the pressure equation. In the modified QUICK, grid weighting factors have been included to account for the non-uniformity of the grid system and more accurately represent the convective terms in the discretized N-S equations. Details regarding the code can be found in Perng and Street.[12]

Conditions of Simulation

A nonuniform grid of 35 × 35 × 20 (20 points in the spanwise direction) was used to simulate the isothermal, forced convection flows in only half of the actual cavity (from the symmetry plane to the endwall). The adequacy of a half-cavity simulation was confirmed by performing a full cavity simulation with a 33 × 33 × 35 nonuniform grid and observing that the resulting vector plots were perfectly symmetric about the symmetry plane. Therefore, by taking advantage of this property, we were able to significantly reduce our computational costs.

Code Verification

Figure 4 allows a comparison of the experimentally measured and numerically simulated horizontal (U) and vertical (V) velocities along the vertical ($X = 0$) and horizontal ($Y = 0$) center-lines, respectively, of the symmetry ($Z = 0$) plane of a cavity of SAR = 1:1. During experiments, the flow was allowed to attain a fully-developed state (the flow never does reach a complete steady-state) and then velocities were measured using the LDA system. Using SEAFLOS1-I, a time-accurate solution (starting from rest) of the first 13 minutes of the flow was obtained. The simulated velocity profiles in Figure 4 represent the mean values based on the flow field during the time period of 7 to 10 minutes after start-up. We readily observe that the comparison is excellent.

In order to confirm that the simulation also reproduces the salient flow features, the visualization pictures obtained for the plane $X = 0.37$ (ie. a plane 20 mm from the DSW and parallel to it) may be compared with a particle-track ("exposure-time" = 8 sec.) plot of the simulated results at a time of 9 minutes after start-up. From the simulated results in Figure 5 and the visualization picture in Figure 6(b), we observe that the model succeeds in accurately simulating the size and location of the important flow features such as the TGL vortices and the corner vortices.

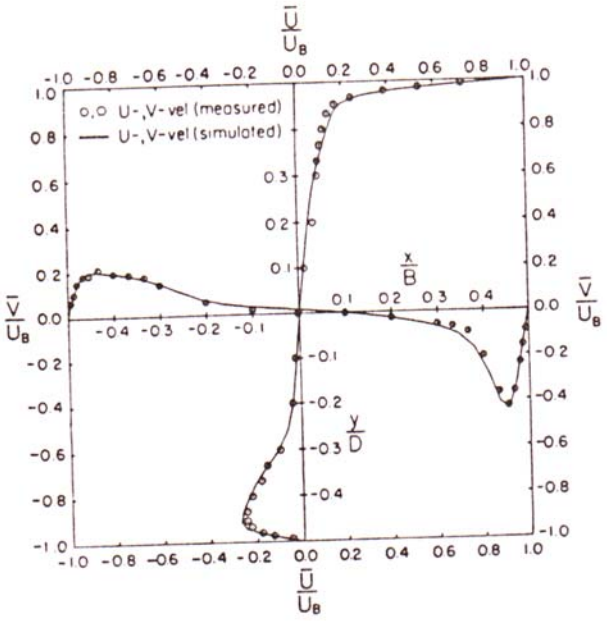

Figure 4 Normalised, mean U- and V-velocity profiles, from measurements, and simulation (SAR=1:1) for symmetry (Z=0) plane

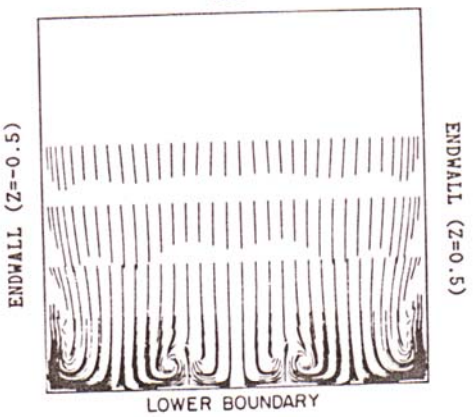

Figure 5 Particle-tracks from simulation (SAR=1:1, Plane X=0.37, t=540 sec.)

In addition to the flow at an SAR of 1:1 and $Re = 3200$, we also observed a close agreement between measured velocity profiles and visualization pictures, and the corresponding profiles and particle track plots from the simulations for flows at SAR's of 0.5:1 and 0.25:1 and $Re = 3200$. This leads us to believe that the SEAFLOS1-I scheme is an ideal complement to the physical experiment program and can, therefore, play a major role in characterising the complexities of these flows.

Observations

The Downstream Secondary Eddy

From Figure 6(a), one can infer the location of the "separation" line on the Downstream Side Wall (DSW; plane $X = 0.5$), which is the locus of points at which the fluid descending along the wall separates from it. As this fluid approaches the lower boundary the adverse pressure gradient due to this solid surface results in a reduction in the vorticity being advected down the wall in the boundary layer. At some distance from the lower boundary, the net vorticity is zero (see Figures 7(a) and (b)), and the fluid separates, resulting in a secondary corner eddy (the DSE). The question, therefore, arises as to why the "separation point" is higher in the region of the corner and TGL vortices.

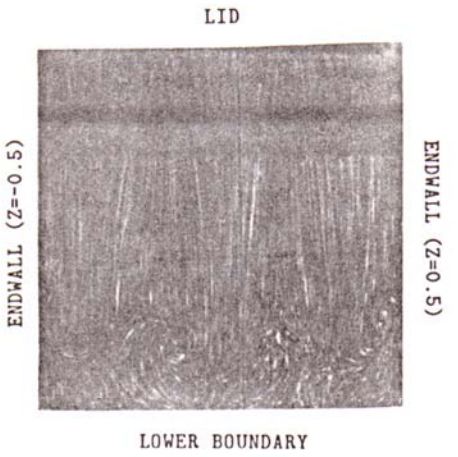

(a) 5 mm from DSW (Plane X=0.47)

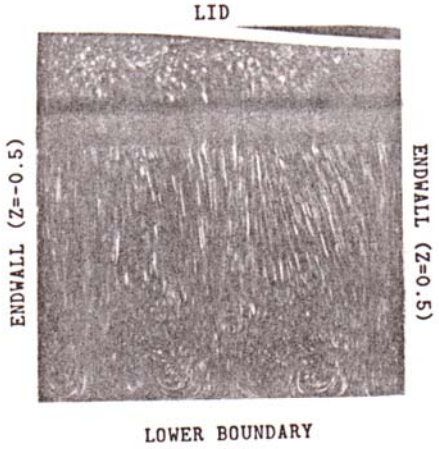

(b) 20 mm from DSW (Plane X=0.37)

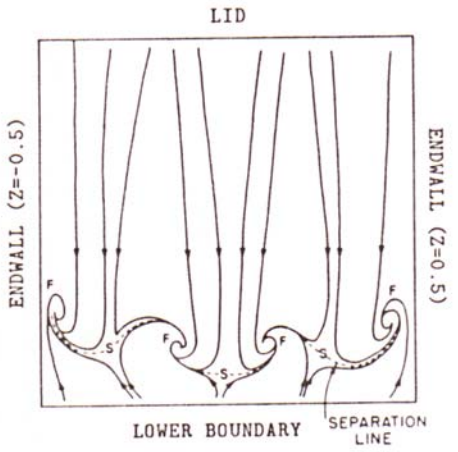

(c) Phase-plane interpretation of 6(a)

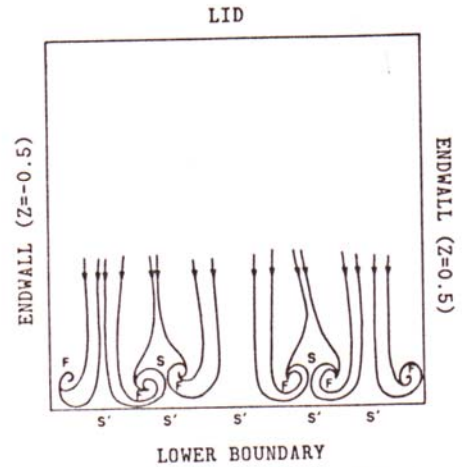

(d) Phase-plane interpretation of 6(b)

Figure 6 Flow Visualization (SAR=1:1) at various distances from the DSW and their phase-plane interpretations

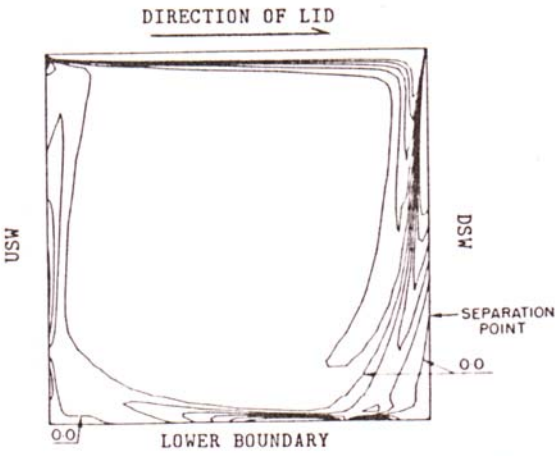

(a) TGL vortex pair occurs outside symmetry plane, t=540 sec.

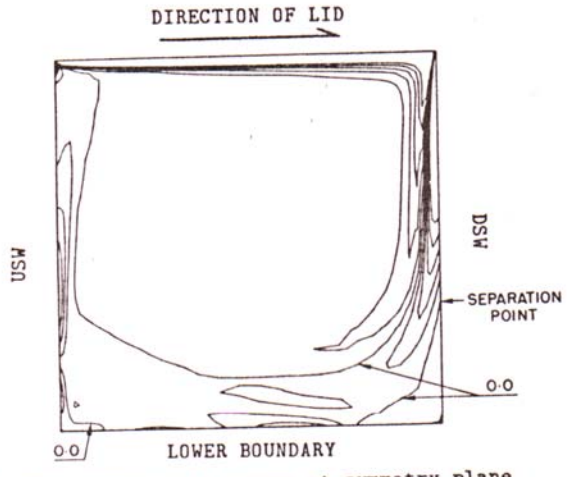

(b) TGL vortex pair occurs at symmetry plane, t=600 sec.

Figure 7 Vorticity contours from simulation (SAR=1:1) at the symmetry (Z=0) plane, for two different spanwise locations of the TGL vortices

Figure 6(a) provides us with some clues. From this picture, it appears that the corner and TGL vortices are inducing spanwise motions in the DSE resulting in the entrainment of the fluid in the DSE into the vortical structures. These spanwise motions reduce the effect of the adverse pressure gradient in the region between the vortices because they bleed away fluid of vorticity opposite in sign to that of the descending boundary layer, thus causing a lower "separation point" in this region. Furthermore, by comparing Figures 6(a) and (b), it is apparent that not only is the motion spanwise in the region immediately behind the TGL vortices, but a strong "upwash" is also evident. This "upwash", then, acts in the same sense as the adverse pressure gradient, augmenting the opposing vorticity on the DSW, and causing the separation to occur higher up on the DSW. Figures 7(a) and (b) show the distribution of vorticity from our simulations, without and with the presence of a TGL vortex pair in the symmetry plane. We observe that the presence of a vortex pair pushes the null-vorticity contour higher up on the DSW, which lends support to our hypothesis. In addition, the fluid adjacent to the endwalls separates earlier, because it faces deceleration caused by not one, but two walls. It may be concluded, therefore, that the size of the DSE is greatest in the immediate region of the endwalls, and in the regions where the TGL vortices are present. This is certainly the case for SAR's of 1:1 and 0.5:1.

This same explanation also accounts for the larger-sized DSE observed in the symmetry plane in the cavity of SAR of 0.25:1, which is counter to the trend reported by Koseff and Street[8] at SAR's of 1:1 and 2:1 (see Introduction). At this very small SAR, no TGL vortices are present. Furthermore, the corner vortices seem to be weaker (Figure 9), and are unable to entrain substantial quantities of fluid from the DSE. Thus, the effect of the adverse pressure gradient along the DSW is not reduced by spanwise "bleeding", resulting in an earlier separation, and consequently, a larger DSE.

Critical point theory provides us with an alternative means of studying the DSE region. Although Figures 6(a) and (b) show that the flow in the lid-driven cavity is extremely complex, certain "critical points" can be readily discerned in these visualizations. Perry et al.[13] define a critical point as "a point in a flow field at which the instantaneous streamline slope is indeterminate." In 2-d flows, critical points occur in the form of centers and saddles, while in 3-d flows, foci and nodes are also found.

Figure 6(c) and (d) are hand-drawn phase portraits of the flows in Figures 6(a) and (b) respectively. Saddles are marked as "S", foci as "F", and surface- (or half-) saddles as "S'". Figure 6(c) shows the streamlines (actually, pathlines; however, given the slowly-varying nature of the flow, we use these terms interchangeably for the purposes of this discussion) in a plane ($X = 0.47$) 5 mm away from the DSW. In this plane, the phase portrait is quite symmetric. We have a saddle in the symmetry plane, and one more on either side. All the separatrices (trajectories that emanate from the saddles) end up in foci, one of which is located on either side of each saddle. Connecting the critical points in Figure 6(c) by a smooth curve produces the "separation" line. The fluid elements above this line have a downward component of velocity, while below the line, the reverse is true. Obviously, these fluid elements that move upwards belong to the DSE. Therefore, we see that the DSE varies quite significantly in size as a function of the spanwise co-ordinate.

Figure 6(d) is a phase portrait of the flow in a plane ($X = 0.37$) 20 mm away from the DSW, and a comparison with Figure 6(c) shows an interesting evolution of the streamlines, and the associated critical points. The flow still retains most of its symmetric character. The two outer foci of Figure 6(c) have now descended to the lower boundary of the cavity and form the corner vortices. This results in the formation of surface saddles (stagnation points) adjacent to the corner vortices, which in turn perturb the flow sufficiently to create two new foci. Each of these combines with the previously existing ones (the inner two foci of Figure 6(c)) indicating two pairs of TGL vortices. By superimposing Figure 6(d) on (c), we see that very close to the endwalls (the planes $Z = 0.5$ and $Z = -0.5$) and directly above the TGL vortex pairs, the separation occurs earlier, resulting in a large-sized DSE. Conversely, in the regions above the two outer, and the central surface saddles, the DSE is smaller.

The Taylor-Görtler-Like vortices

The preceding section demonstrates that the TGL vortices interact strongly with the DSE. At large SAR (2:1 or 3:1), the TGL vortex pairs display a significant degree of unsteadiness. That is, they vary in number and meander in the spanwise direction (Koseff and Street, 1984a). As the SAR is reduced, both these trends are suppressed. At an SAR of 1:1, the TGL pairs do exhibit a meander, but almost always only two pairs are observed (Figure 6(b)). At an SAR of 0.5:1 only one pair, which is "locked" in position and bisected by the symmetry plane, is observed (Figure 8, visualization plane $X = 0.37$). The immobility of this pair was confirmed by examining a sequence of photographs (taken at 15 second intervals over several minutes) and noting that the flow pattern was virtually unchanged. Finally, at an SAR of 0.25:1, the TGL vortex pairs do not form at all; instead the two corner vortices completely occupy the span of the cavity (Figure 9, visualization plane $X = 0.37$); these, again, are very stable.

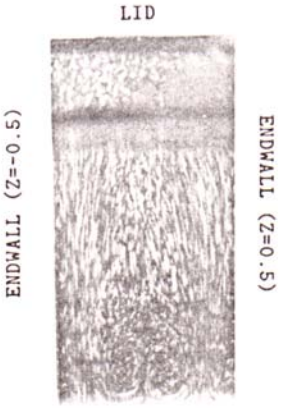

Figure 8 Flow visualization (SAR=0.5:1, Plane X=0.37)

Figure 9 Flow visualization (SAR=0.25:1, Plane X=0.37)

Figures 10(a) and (b) demonstrate one of the effects of a TGL vortex pair on the overall flow. Figure 10(a) is a visualization of the symmetry ($Z = 0$) plane for an SAR of 0.5:1 (ie, this plane now bisects a TGL vortex pair, and is therefore most strongly affected by it), while Figure 10(b) is a view of the symmetry plane at an SAR of 0.25:1 (no TGL vortices present). In Figure 10(a) it can be seen that the DSE has ruptured. Now, the TGL vortices entrain both the fluid moving down the DSW as well as the low momentum fluid contained in the DSE. The resulting stream has a strong upward component into the core of the cavity. In contrast, Figure 10(b) shows that in the absence

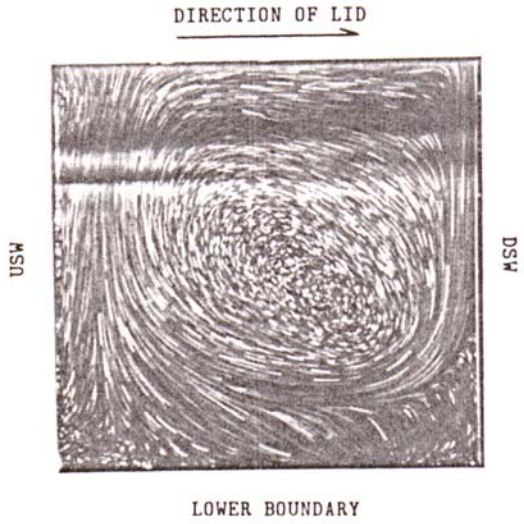

Figure 10(a) Flow Visualization at the symmetry (Z=0) plane, SAR=0.5:1

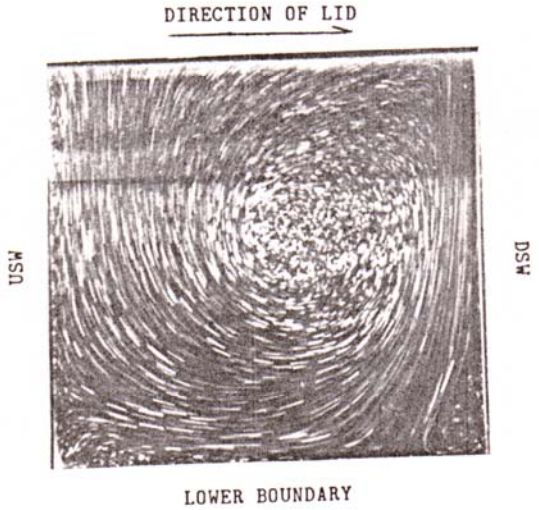

Figure 10(b) Flow Visualization at the symmetry (Z=0) plane, SAR=0.25:1

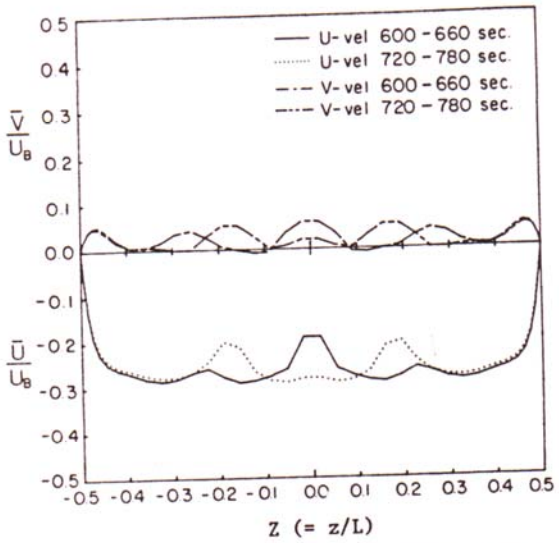

Figure 11 Spanwise variation of U and V-velocities from simulation (SAR=1:1) along the line Y=-0.45 in the plane X=0

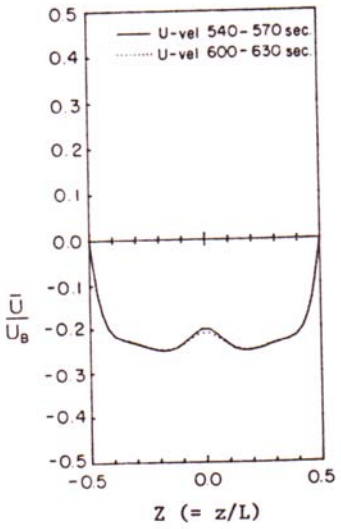

Figure 12 Spanwise variation of U-velocity from simulation (SAR=0.5:1 along the line Y=-0.45 in the Plane X=0

of the TGL vortices, the fluid flowing over the DSE, continues parallel to the lower boundary of the cavity, without an upward tilt.

This suggests that by examining the spanwise variation of the U- and V-velocities, close to the lower boundary of the cavity, the location of a TGL vortex pair could be detected by a drop in the magnitude of the U-velocity and a corresponding rise in the V-velocity. Figure 11 displays the spanwise U- and V-velocity profiles, calculated from our numerical simulations, for an SAR of 1:1, averaged over two one-minute periods (10-11 and 12-13 minutes after start-up) and at a distance of 7 mm above the lower boundary. In our co-ordinate system, this corresponds to the line $Y = -0.45$ in the plane $X = 0$. This location was chosen because it coincides with the peak in the U-velocity profile along the vertical center-line (Figure 4). The "wake" effect of the TGL pair is obvious from Figure 11–each region of U-velocity deficit (lower magnitude) corresponds to the location of a TGL vortex pair, with matching peaks in the V-velocity profile. In addition, this figure reveals the unsteadiness of the flow due to the spanwise meander of the TGL vortices. However, Figure 12 shows the contrasting nature of the flow at an SAR of 0.5:1. This is a plot of the simulated spanwise variation of the U-velocity, at 9 and 10 minutes after start-up, each representing a 30 second average. The two interesting features of this plot are: first, there is almost no variation of the profile with time, indicating a relatively steady nature, and second, the "wake" effect is not as strong as in the case of higher SAR.

The meandering nature of the TGL vortices at an SAR of 1:1 is further demonstrated in Figure 13 by means of vorticity contours obtained from our simulations. These contours represent curves of constant vorticity in the $X = 0$ plane at two instants of time: 10 and 12 minutes after start-up. The substantial difference in the location of the vortex centers in the two plots provides evidence for the unsteadiness of the flow at this SAR.

The effect of the meandering of the TGL vortices on the mean and rms velocities was obtained by conditionally sampling the experimentally measured velocity at a location 7 mm above the lower boundary, at the symmetry plane of a cavity of an SAR of 1:1 (ie, the point (0,-0.45,0)). This was done as follows: First the maximum V-velocity (V_{max}) in the entire record (5.46 minutes at 100 Hz) was determined. Next, a cut-off fraction was chosen and the data was separated into two categories–(i) "higher": those data points whose V-velocities exceeded the product of V_{max} and the cut-off fraction, and (ii) "lower": those that did not. Therefore, the first category isolates data-points

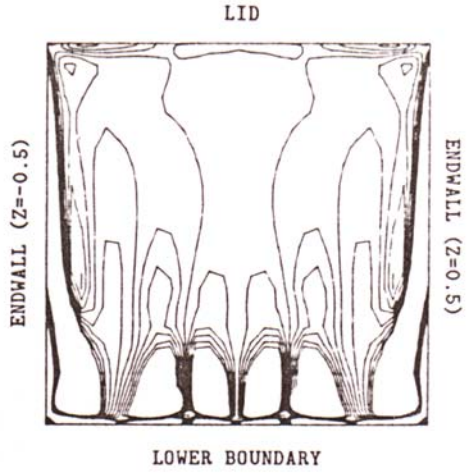

(a) Two pairs of TGL vortices at t=540 sec.

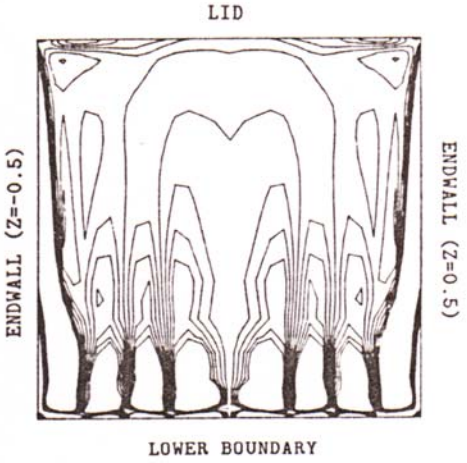

(b) Three pairs of TGL vortices at t=600 sec.

Figure 13 Vorticity contours from simulation (SAR=1:1, Plane X=0.37) at two different times, showing unsteady nature of TGL vortices

that were affected by the TGL vortices. Naturally, as the cut-off fraction increases, this isolation becomes more acute. The local mean and rms values for the U-velocity component were then calculated as was the Reynolds shear stress for each of the two categories. Table 1 summarizes our calculations for four different cut-off fractions: 0.3, 0.4, 0.5 and 0.6. Certain trends are immediately apparent from Table 1:

1. The mean U-velocity is consistently smaller when the V-velocity is high. This agrees with the simulated velocity profiles in Figure 11.
2. The difference between the rms velocities in the two categories increases substantially as the cut-off fraction is increased. At small cut-off values, a larger fraction of the data-points is included in the "higher" category. Therefore, the "lower" category contains only those points that are least affected by the TGL vortices. As a result, the fluctuations are smaller leading to a lower value of the rms velocity. However, as the cut-off value is increased, more data-points are moved from the "higher" to the "lower" category, including those affected by the TGL vortices. This results in a wider variation of the U-velocities and an increase in the calculated rms velocity.
3. An identical argument can be used to explain the trend in the variation of the shear stress with the cut-off fraction.

These observations provide further quantitative evidence that the TGL vortex pairs are not stationary, but meander in a spanwise direction in and out of the plane of observation at an SAR of 1:1. However, when the same analysis is performed on the velocity measured in a similar location in the cavity of SAR of 0.5:1 (Table 2), no substantial differences are evident in the calculated mean and rms velocities, and the shear stress as a function of the cut-off fraction. This therefore substantiates our pictorial evidence that at an SAR of 0.5:1, the TGL vortex pair is "locked" into position, resulting in a relatively steady flow.

Summary and Conclusions

Previous studies by Koseff and Street[3,7,8] and Freitas et al.[9,10] identified two necessary conditions for the existence of TGL vortices in the lid-driven cavity flow: a concave separation surface, and the presence of perturbations. The concave separation surface of the DSE provides the necessary amplification of the perturbations (see Görtler[14]) which are produced by the Taylor instability present at start-up (see Koseff and Street,[3]) and the endwalls (the planes $Z = 0.5$ and $Z = -0.5$) in the physical experiments, and by the endwalls only in the numerical simulations, leading to the formation of the TGL vortices. The numerical simulations of Kim and Moin[15] demonstrate very nicely why no TGL vortices form without the necessary perturbations. Their 3-d simulation was performed using periodic boundary conditions in the spanwise direction instead of endwalls. It was only when a small random perturbation was added to the flow that the TGL vortices

Cut-Off Fraction	0.3	0.4	0.5	0.6
Fraction of time V-vel. > Cut-off	0.328	0.274	0.177	0.054
Lower Mean U-vel	-5.87	-5.73	-5.46	-5.18
Higher Mean U-vel	-3.48	-3.37	-3.36	-3.44
Lower U-vel rms	0.547	0.741	1.03	1.21
Higher U-vel rms	0.515	0.440	0.399	0.384
Lower Shear Stress	0.086	0.194	0.423	0.642
Higher Shear Stress	0.038	0.003	-0.009	-0.007

All velocities in (mm/s); shear stress in $(mm/s)^2$
"Lower" implies V-velocity is below Cut-off
"Higher" implies V-velocity is above Cut-off

Table 1: Variation of Mean and rms U-velocities and shear stress for SAR 1:1

Cut-Off Fraction	0.3	0.4	0.5	0.6
Fraction of time V-vel. > Cut-off	0.817	0.512	0.213	0.056
Lower Mean U-vel	-4.60	-4.61	-4.63	-4.64
Higher Mean U-vel	-4.65	-4.68	-4.71	-4.74
Lower U-vel rms	0.169	0.169	0.172	0.175
Higher U-vel rms	0.177	0.179	0.183	0.189
Lower Shear Stress	- 0.0004	-0.001	-0.003	-0.004
Higher Shear Stress	-0.004	-0.002	-0.001	0.001

All velocities in (mm/s); shear stress in $(mm/s)^2$
"Lower" implies V-velocity is below Cut-off
"Higher" implies V-velocity is above Cut-off

Table 2: Variation of Mean and rms U-velocities and shear stress for SAR 0.5:1

formed. The Taylor instabilities, like the TGL vortices, cannot form in the absence of perturbations. In our numerical simulation, the only three-dimensional perturbations arise from the endwalls. In the few seconds after start-up, these perturbations are unable to propagate in the spanwise direction to a significant degree. Consequently, the Taylor instabilities which are seen during the first 30 seconds after start-up in the physical experiment, are not picked up by the numerical simulations.

In this present study, we have identified a third necessary condition, viz., a sufficiently large aspect ratio. For a given Re, the TGL vortex pair has a preferred spanwise extent, or "wavelength". Figure 8 indicates that this wavelength is about one half of the span of a cavity of SAR 0.5:1. Therefore, in a cavity of SAR 1:1, we have two pairs (Figure 6(b)), while at an SAR of 0.25:1, the TGL vortices are completely suppressed (Figure 9). The number and size of the TGL vortices is also strongly dependent on the Re (which is an indication of the velocity with which the fluid moves over the concave separation surface). The present discussion refers to the $Re = 3200$ case only.

This study has also shown that there is a strong interaction between the DSE, the TGL vortices and the corner vortices, which produces much of the unsteadiness observed in the flow. At SAR greater than 0.5:1, the TGL vortices meander in the spanwise direction and form in different spanwise locations. These vortices entrain fluid from the DSE, influencing, therefore, not only the spanwise variation in the size of this eddy, but also the temporal variation in its size. The TGL vortices entrain low momentum fluid from the DSE resulting in "wake-like" regions in the spanwise U-velocity profiles. These regions move as the TGL vortices move effectively distributing the lower U-momentum/ higher V-momentum in both the spanwise and vertical directions. This process combined with the damping action of the endwalls results in a overall "weakened" (as compared to 2-d simulations) motion in the cavity.

At an SAR of 0.5:1, much of the unsteadiness observed at the higher SAR values disappears. The TGL vortex pair is "locked" in position and the size of the DSE at the symmetry plane is fairly constant in time. This occurs, we believe, because the weaker (overall motion in the cavity is weaker due to endwall effects) TGL vortices entrain less fluid from the DSE resulting in a more stable eddy structure. The fact that the "wake" is much smaller in the U-velocity profile certainly seems to suggest this.

From the above discussion it is clear that the endwalls are an important influence on the flow. A qualititive study on the effect of the endwalls has been performed by Koseff and Street[8] and a more quantitative study by Prasad and Koseff.[16] This study which covers Re's from 3200 to 10,000 and SAR's from 0.5:1 to 3:1 provides further evidence on the unsteadiness of the this flow.

Acknowledgements

The supports of the Department of Energy under Grant DE-FG03--84ER13240 and of the National Science Foundation under Grant MSM-83-12061 are gratefully acknowledged. The authors express their gratitude to Prof. R.L. Street, who not only supervised the development of the SEAFLOS1 code, but has been the guiding spirit behind the Environmental Fluid Mechanics Laboratory. They also thank Prof. S.G. Monismith, and Dr. S.G. Schladow for their helpful comments and criticisms.

References

[1] De Vahl Davis, G. and Mallinson, G.D., "An Evaluation of Upwind and Central Difference Approximations by a Study of Recirculating Flow," *Computers and Fluids*, Vol. 4, 1976, pp. 29-43.

[2] Tuann, S.-Y. and Olson, M.D., "Review of Computing Methods for Recirculating Flows," *Journal of Computational Physics*, Vol. 29, 1978, pp. 1-19.

[3] Koseff, J.R. and Street, R.L., "Visualization Studies of a Shear Driven Three-dimensional Recirculating Flow," *Journal of Fluids Engineering*, Vol. 106, 1984, pp. 21-29.

[4] Ghia, U., Ghia, K.N. and Shin, C.T., "High-Re Solutions for Incompressible Flow using Navier-Stokes Equations and a Multigrid Method," *Journal of Computational Physics*, Vol. 48, 1982, pp. 387-411.

[5] Olson, M.D. and Tuann, S.-Y., "Further Finite Element Methods for the Square Cavity," *Proc. 3rd Intl. Conf. Finite Elements in Flow Problems*, Banff, Alberta, Canada, 1980, pp. 143-152.

[6] Nallasamy, M. and Krishna Prasad, K., "On Cavity Flow at High Reynolds Numbers," *Journal of Fluid Mechanics*, Vol. 79, 1977, pp. 391-414.

[7] Koseff, J.R. and Street, R.L., "The Lid-Driven Cavity Flow: a Synthesis of Qualitative and Quantitative Observations," *Journal of Fluids Engineering*, Vol. 106, 1984, pp. 390-398.

[8] Koseff, J.R. and Street, R.L., "On End Wall Effects in a Lid-Driven Cavity Fiow," *Journal of Fluids Engineering*, Vol. 106, 1984, pp. 385-389.

[9] Freitas, C.J., Findikakis, A.N. and Street, R.L., "The Physics of a Three-dimensional Cavity Flow," *Proc. 4th Intl. Conf. on Numerical Methods in Laminar and Turbulent Flow*, Univ. of Wales, Swansea, U.K., July 9-12, 1985.

[10] Freitas, C.J., Street, R.L., Findikakis, A.N. and Koseff, J.R., "Numerical Simulation of Three-dimensional Flow in a Cavity," *International Journal of Numerical Methods in Fluids*, Vol. 5, 1985, pp. 561-575.

[11] Rhee, H.S., Koseff, J.R. and Street, R.L., "Flow Visualization of a Recirculating Flow by Rheoscopic Liquid and Liquid Crystal Techniques," *Experiments in Fluids*, Vol. 2, 1984, pp. 57-64.

[12] Perng, C.-Y., and Street, R.L., "Three-Dimensional Unsteady Flow Simulations: Alternative Strategies for a Volume-Averaged Calculation," *International Journal for Numerical Methods in Fluids* in press.

[13] Perry, A.E., Lim, T.T and Chong, M.S., "The Instantaneous Velocity Fields of Coherent Structures in Coflowing Jets and Wakes," *Journal of Fluid Mechanics*, Vol. 101, Part 2, 1980, pp. 243-256.

[14] Görtler, H., "On the Three-dimensional Instability of Laminar Boundary Layers on Concave Walls," *NACA Technical Memorandum 1375*, 1954.

[15] Kim, J. and Moin, P., "Application of a Fractional-step Method to Incompressible Navier-Stokes Equations," *Journal of Computational Physics*, Vol. 59, 1985, pp. 308-323.

[16] Prasad, A.K., and Koseff, J.R., "Reynolds Number and End--Wall Effects in a Lid-Driven Cavity Flow," submitted to *Physics of Fluids*.